

SCIENTIFIC REPORTS

OPEN

Design of Hydrogen Storage Alloys/Nanoporous Metals Hybrid Electrodes for Nickel-Metal Hydride Batteries

Received: 18 December 2015

Accepted: 20 May 2016

Published: 07 June 2016

M. M. Li, C. C. Yang, C. C. Wang, Z. Wen, Y. F. Zhu, M. Zhao, J. C. Li, W. T. Zheng, J. S. Lian & Q. Jiang

Nickel metal hydride (Ni-MH) batteries have demonstrated key technology advantages for applications in new-energy vehicles, which play an important role in reducing greenhouse gas emissions and the world's dependence on fossil fuels. However, the poor high-rate dischargeability of the negative electrode materials—hydrogen storage alloys (HSAs) limits applications of Ni-MH batteries in high-power fields due to large polarization. Here we design a hybrid electrode by integrating HSAs with a current collector of three-dimensional bicontinuous nanoporous Ni. The electrode shows enhanced high-rate dischargeability with the capacity retention rate reaching 44.6% at a discharge current density of 3000 mA g⁻¹, which is 2.4 times that of bare HSAs (18.8%). Such a unique hybrid architecture not only enhances charge transfer between nanoporous Ni and HSAs, but also facilitates rapid diffusion of hydrogen atoms in HSAs. The developed HSAs/nanoporous metals hybrid structures exhibit great potential to be candidates as electrodes in high-performance Ni-MH batteries towards applications in new-energy vehicles.

Recently, with increasing pressures of environmental problems and energy crisis, more and more sights have turned to new-energy vehicles^{1–3}. A series of advanced battery technologies have been emerged for applications in this field, nickel metal hydride (Ni-MH) batteries, Li-ion batteries, proton exchange membrane fuel cells etc^{4–6}. Ni-MH batteries were first commercialized and they were facing great challenges from Li-ion batteries over the past few years. Nonetheless, Ni-MH batteries still hold an important position in the market, especially in hybrid electric vehicles, due to their superior safety even under abuse conditions, temperature adaptability and environmental friendliness^{7–9}. Moreover, Ni-MH batteries have also been widely used in the fields of power tools and modern military devices^{10,11}. A moderate energy density is sufficient while a high power density is critical for these applications. To meet the marketing requirements for high-power Ni-MH batteries, one has to enhance the high rate dischargeability (HRD) properties of their negative electrode materials—hydrogen storage alloys (HSAs), which determine the power density of Ni-MH batteries. It should be noted that although supercapacitors have high power density, the low energy density at present makes it only a complement to batteries in energy storage devices¹².

In the last two decades, various approaches have been proposed to improve the electrochemical properties of HSAs, such as composition optimization¹³, surface modification^{14,15}, preparation techniques modification¹⁶, processing methods optimization¹⁷ etc. The surface modification has been demonstrated as an efficient approach to enhance the HRD performance of HSAs. The traditional surface modification methods, such as acid, alkaline and fluorination treatments, could dissolve rare earth oxides or hydroxides on the surface of alloy particles. The active elements (for example, Al and Mn) are also etched to form a Ni-rich porosity layer, which is useful for accelerating the electrochemical reaction rate^{14,15}. Several groups have reported the improvements in HRD of alloy electrodes by microencapsulating alloy particles with various coating layers, Ni, Cu, Co, Ni-P, and so on, via the electroless technic^{18–25}. It was reported that the plated Cu and Ni could act as microcurrent collectors to increase the charge transfer rate on electrode surfaces and as barriers to protect alloy particles from oxidation^{18,19}. The Ni-Co deposits

Key Laboratory of Automobile Materials (Jilin University), Ministry of Education, and School of Materials Science and Engineering, Jilin University, Changchun 130022, China. Correspondence and requests for materials should be addressed to C.C.Y. (email: ccyang@jlu.edu.cn) or Q.J. (email: jiangq@jlu.edu.cn)

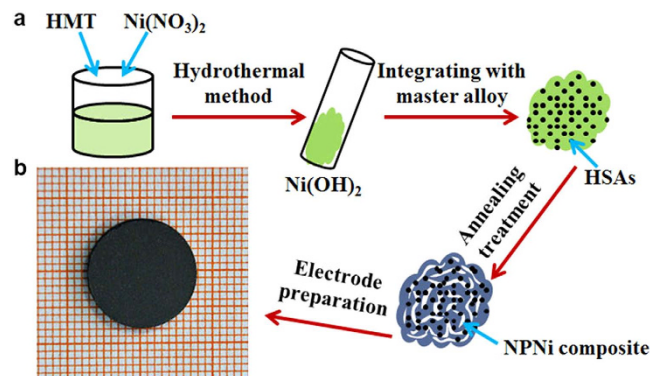


Figure 1. A schematic illustration of the preparation of HSAs/NPNi composite by using a top-down method. (a) The preparation process of the HSAs/NPNi composite. (b) The photograph of an electrode pellet for electrochemical measurements.

could work as catalysts to improve the electric catalytic activity of HSAs²³. Moreover, the electroless plating of Ni-P nanoparticles on alloy surfaces has been demonstrated to be beneficial for decreases of contact resistance and charge transfer resistance of the electrode²⁵. Mechanical milling has also been introduced to improve the HRD of hydride electrodes²⁶. Moreover, carbon nanotube, graphite, and nickel nanoparticles were added into HSAs to form hybrid electrodes^{27–29}. Note that the hybrid electrode is prepared by compositing two or more different materials (in general, at least one constituent is at the nanometer scale) into a single electrode and it shows new properties not necessarily found in the individual parent components. The additives show remarkable positive effects on accelerating the absorption and desorption of hydrogen atoms, increasing the electrochemical reaction rate²⁷. All these modification methods have been proved to be effective in improving the HRD performance of hydride electrodes, but the improvements are limited^{26,27}. Moreover, they bring some disadvantages, for example, the deformation and amorphization of HSAs²⁶. The current commercial Ni-MH battery in hybrid electric vehicles only deliver the specific power of 150–400 W/kg, which cannot satisfy the increasing marketing requirements^{8,30}. The Department of Energy of US has set a target of over 650 W/kg³¹. Thus, it is urgent to explore the intrinsic factor that dominates the HRD properties of HSAs, and to develop novel materials to achieve the above target.

Conventionally, the metal hydride electrodes for electrochemical measurements are prepared by cold pressing the mixture of HSA powders and copper or nickel powders (as current collector and binder)²⁷. In this regard, a large contact resistance (R_C) between current collector and active materials, or within active materials, a large charge transfer resistance (R_{CT}) and a large mass transport resistance (R_{MT}) exist during the electrochemical reaction of electrodes³². The large internal resistances lead to large polarization and poor electrochemical properties. Recently, nanoporous metals have demonstrated potential technological advantages to reduce the above internal resistances due to their unique porous structures with large surface/volume ratio^{32,33}, which have been successfully used in supercapacitors³⁴, electrochemical catalysts^{35,36}, Li-ion batteries³⁷ and other energy storage devices³⁸. The HRD performance of a metallic hydride electrode is mainly determined by two steps: the electrochemical reaction on the surface of alloy electrode (charge transfer process) and the diffusion of absorbed hydrogen into the alloy bulk (hydrogen diffusion process)³⁹. These two steps are closely related to exchange current density (I_0), electrochemical impedance and hydrogen diffusion coefficient (D_H). A higher I_0 value corresponds to a better kinetics of absorbed and desorbed hydrogen, a smaller polarization resistance and a faster charge transfer process⁴⁰. A larger D_H allows for a faster transportation of absorbed hydrogen and a faster hydrogen diffusion process. Nanoporous metals have unique porous structures with large surface/volume ratio. Hence, they could be used to (i) increase the electrochemical active area and thus to improve electrochemical reaction kinetics; and (ii) decrease the internal resistance and polarization and thus to enhance the conductivity of a metallic hydride electrode. Integrating nanoporous metals with HSAs powders is expected to enhance the HRD performance of HSAs. This approach has not been reported before and it opens a door to applications of nanoporous metals in Ni-MH batteries.

The major aim of this work is to develop a new type of hybrid electrode (HSAs/NPNi) by incorporating HSAs powders with a current collector of three-dimensional bicontinuous nanoporous Ni for applications in Ni-MH batteries. Such a composite shows excellent HRD performance where its discharge capacity is 2.4 times that of the bare HSAs at a discharge current density of 3000 mA g⁻¹. It is found that the NPNi introduced into the composite decreases R_C and R_{CT} , and accelerates the diffusion rate of hydrogen atoms in HSAs. The findings in this work provide a new strategy to improve the HRD performance of Ni-MH batteries, which can also be utilized to design other electrode materials.

Results and Discussions

The HSAs/NPNi hybrid electrode pellets were fabricated with a facile procedure, which involves hydrothermal synthesis of Ni(OH)₂, integration of Ni(OH)₂ with the master alloy (LaCe)_{0.9}Y_{0.1}Ni_{3.7}Co_{0.75}(MnAl)_{0.65}, thermal reduction of Ni(OH)₂ by annealing treatment of the composites under an Ar/H₂ atmosphere, and cold pressing the mixture of as-prepared composites and carbonyl nickel powders (Fig. 1a,b). Figure 2a shows X-ray diffraction (XRD) patterns of the master alloy and the composite. It is evident that the master alloy retains a typical

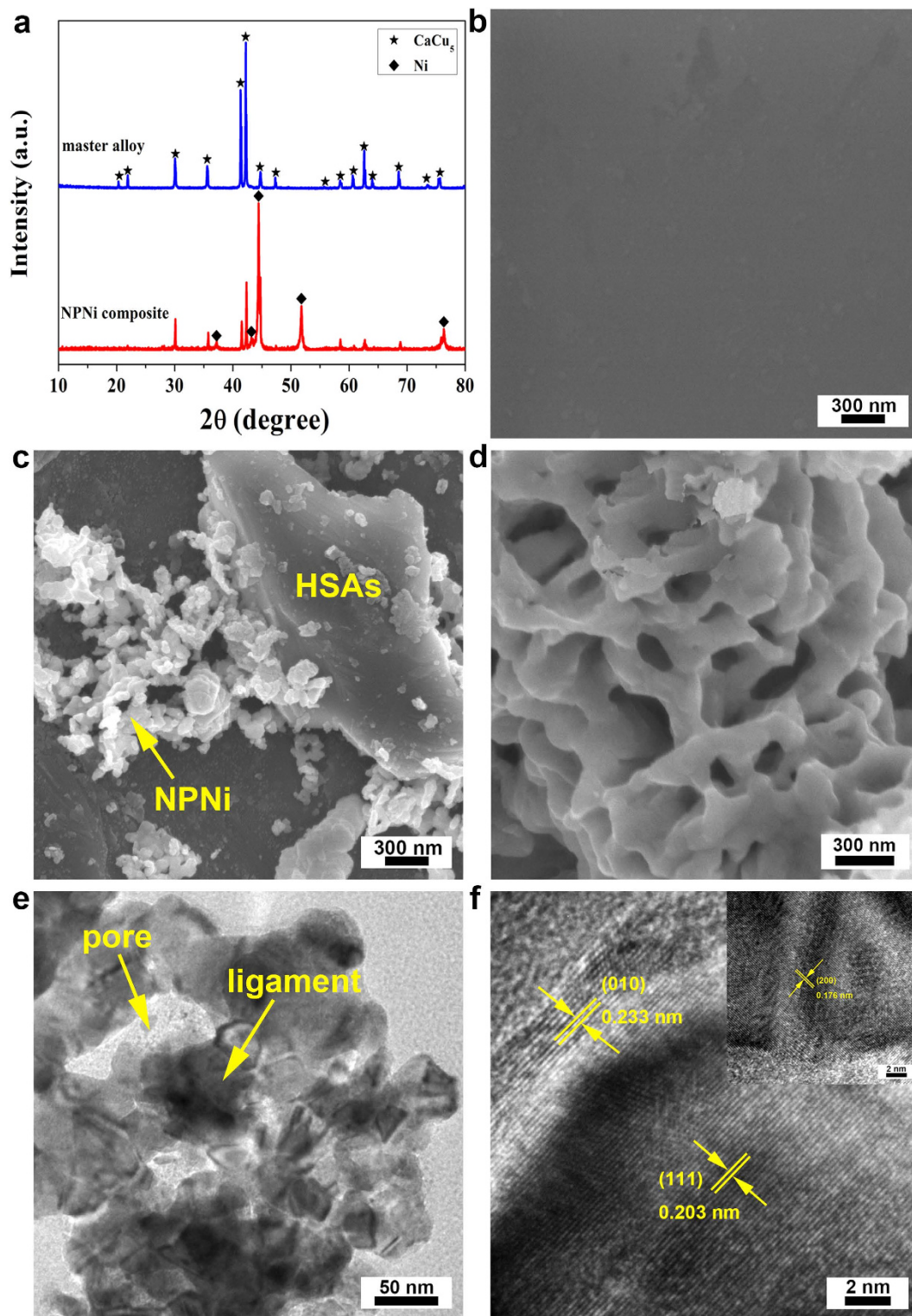


Figure 2. Morphological and microstructure characterizations of the master alloy and HSAs/NPNi composite. (a) XRD patterns of the master alloy and HSAs/NPNi composite. (b–d) are top-view SEM images of surfaces of the master alloy, composite and NPNi, respectively. (e, f) (including the inset) are TEM and HRTEM images of NPNi.

CaCu_5 -type crystalline structure with a space group of $P6/mmm$ ⁴¹. The XRD pattern of the composite shows characteristic peaks of Ni besides the LaNi_5 phase. Moreover, it is found that the peaks of Ni phase are broadened, which is attributed to the formation of nanoscale polycrystals [NPNi as demonstrated by scanning electron

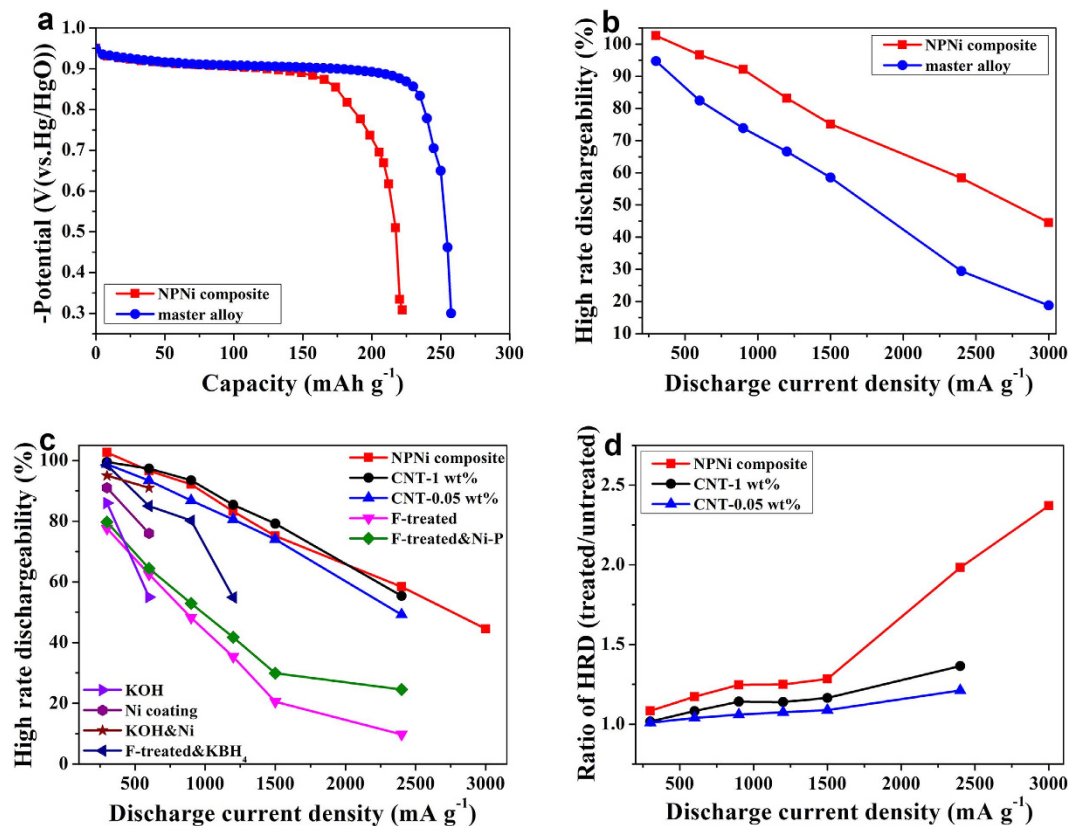


Figure 3. Discharge capacities and HRD properties. (a) The discharge capacity curves of the HSAs/NPNi hybrid electrode and master alloy electrode at room temperature. (b) The HRD properties of the HSAs/NPNi hybrid electrode and master alloy electrode at different discharge current densities measured at room temperature. (c) Comparisons of HRD properties of the HSAs/NPNi composite and reported experimental data of AB₅-type HSAs from other advanced surface modification methods, including carbon nanotube (CNT) doping (CNT-1 wt% and CNT-0.05 wt%) for MmNi_{3.6}Co_{0.7}Al_{0.3}Mn_{0.4}²⁷, fluoridation treatment (F-treated), fluoridation and the following treatment with KBH₄ (F-treated & KBH₄) for MmNi_{3.8}Co_{0.75}Mn_{0.4}Al_{0.2}¹⁵, combination of fluoridation treatment and electroless plating with Ni-P coating (F-treated & Ni-P) for LaNi₄Al²⁵, hot alkaline treatment at 100 °C (KOH), electroless with nickel coating (Ni coating), and combination of alkaline treatment and electroless with Ni coating (KOH & Ni) for MmX_{4.3}(Al_{0.3}Mn_{0.4})_{0.5} (X = Co, Mo, Mn, Al, Cu)¹⁴. (d) A comparison of ratios of HRD performance after treatment to that of untreated HSAs between NPNi incorporation and CNT doping.

microscope (SEM) and transmission electron microscope (TEM) images below] during the annealing treatment⁴². The weight percent of NPNi in the composite is 36.87% as measured by an inductively coupled plasma (ICP) analyzer. Note that the weight percent (y) of original Ni (of master alloy) in the composite is determined by comparing with the contents of La, Ce, Y, Co, Mn and Al. For example, the Co content in the composite was measured by ICP as x ($=6.48\%$) and we have $y = 5.01x = 32.47\%$ (the weight percent ratio of Ni to Co in the master alloy is 5.01). The total Ni content in the composite is $z = 69.34\%$ as measured by ICP. Then, the weight percent of NPNi in the composite ($z - y = 36.87\%$) is obtained. The morphologies of as-fabricated samples are characterized by a field-emission SEM (FESEM) and a TEM. Figure 2b shows an SEM image of the master alloy, where clean surfaces could be observed. On the contrary, as shown in Fig. 2c, the master alloy particle is surrounded by NPNi in the composite, exhibiting rough surfaces. The NPNi with pore size of ~ 200 nm and ligament size of ~ 120 nm is formed during the reduction of Ni(OH)₂ (Fig. 2d). Figure 2e shows a TEM image of NPNi at a low magnification. Combining Fig. 2d,e, we can find that (1) NPNi has a three-dimensional bicontinuous nanostructure; and (2) NPNi ligaments show a hyperboloid-like shape, where a positive curvature forms columnar ligaments while a negative curvature accommodates nanopores^{43,44}. Note that the nanopores and ligaments in nanoporous metals or intermetallics are topologically and morphologically equivalent, i.e., they are inverses in a three-dimensional space, resulting in a near-zero surface curvature on average. Such a structure is typically called bicontinuous structure due to its continuous nanopore channels and ligaments. Figure 2f presents a high-resolution TEM (HRTEM) image of NPNi, in which the interplanar spacings of 0.203, 0.233 and 0.176 nm correspond to (111), (010) and (200) (inset of Fig. 2f) planes of Ni, respectively.

Figure 3a shows the discharge capacity curves of the master alloy electrode and HSAs/NPNi hybrid electrode at a discharge current density of 60 mA g⁻¹ (0.2C). The measured maximum discharge capacity C_{\max} values are 257.51 mAh g⁻¹ and 222.14 mAh g⁻¹ for the master alloy and composite electrodes, respectively, which are listed

Samples	C_{\max} (mAh g ⁻¹)	HRD ₃₀₀₀ (%)	R_c (mΩ)	R_{CT} (mΩ)	I_0 (mA g ⁻¹)	I_L (mA g ⁻¹)	D_H (×10 ⁻¹⁰ cm ² s ⁻¹)
HSAs/NPNi	222.14	44.6	157	265	166.88	3700.98	1.35
master alloy	257.51	18.8	256	336	104.22	2894.90	1.19

Table 1. Electrochemical properties of the HSAs/NPNi hybrid electrode and master alloy electrode.

in Table 1. It is known that the reactions of a metal hydride electrode during charging are typically described by (1) the Volmer reaction: $H_2O + e^- \rightarrow H_{ads} + OH^-$; (2) the transition of hydrogen atoms between adsorbed state and adsorbed state on the surface of alloy particles: $H_{ads} \rightarrow H_{abs}$; and (3) the following phase transformation process: $MH_\alpha \rightarrow MH_\beta$ ³¹. Note that the order of the above reactions is on the contrary during the discharging process. Apart from these reactions, there is also a hydrogen evolution reaction (HER) by the Volmer-Tafel reaction route ($H_2O + e^- \rightarrow H_{ads} + OH^-$ and the following $2H_{ads} \rightarrow H_2$) or by the Volmer-Heyrovsky reaction route ($H_2O + e^- \rightarrow H_{ads} + OH^-$ and the following $H_{ads} + H_2O + e^- \rightarrow H_2 + OH^-$) during charging⁴⁵. It has been demonstrated that NPNi could act as a catalyst to accelerate the HER reaction⁴⁶. As a result, during charging, H_{ads} as a product of the Volmer reaction fast recombined to generate H_2 in the composite, which results in (1) a decrease of the number of H_{ads} to diffuse into the HSAs to create hydrides; and (2) a reduction of the utilization rate of active materials. In this case, during discharging, the reactant H_{ads} ($H_{ads} + OH^- \rightarrow H_2O + e^-$) becomes less, leading to a smaller C_{\max} value of the composite compared with the master alloy. Figure 3b shows the HRD property of the both electrodes. The corresponding electrochemical data are listed in Table 1. The capacity retention rates of the composite electrode are 102.6, 96.6, 92.1, 83.2, 75.2, 58.4 and 44.6% at the discharge current densities of 300, 600, 900, 1200, 1500, 2400 and 3000 mA g⁻¹, respectively, showing better HRD performance than that of the master alloy electrode (the corresponding capacity retention rates are 94.7, 84.4, 73.9, 66.6, 58.5, 29.5 and 18.8%). At the discharge current density of 3000 mA g⁻¹ (10C), the capacity retention rate of the composite is 2.4 times that of the master alloy. As noted above, the C_{\max} value of the composite at 0.2C is lower than that of the master alloy. But the discharge capacity of the former at 10C (98.99 mAh g⁻¹) is twice that of the latter (48.39 mAh g⁻¹). Moreover, it should be noted that the discharge capacity (228.02 mAh g⁻¹) of the composite at 1C (300 mA g⁻¹) is a little larger than the capacity (222.14 mAh g⁻¹) at 0.2C (60 mA g⁻¹). This may result from stronger hydrogen evolution during charging at higher discharge current density (1C) than that at lower current density (0.2C)¹⁹. In the discharging process, the dissolved hydrogen is ionized in the electrolyte and an additional charge contributes to the overall value, causing larger discharge capacity of the composite electrode at 1C than that at 0.2C¹⁹. Note that their difference is very small (5.88 mAh g⁻¹), which indicates that (1) most of hydrogen has escaped from the electrolyte in the open system of a half-cell test; and (2) contributions of the ionization of hydrogen to discharge capacities of the master alloy and composite electrodes are limited although the both electrodes show different catalytic activity for the HER reaction. For a comparison, we have also fabricated the electrode using bare HSAs without annealing under an Ar/H₂ atmosphere and tested its electrochemical properties. It shows larger discharge capacity (302.62 mAh g⁻¹) while poorer HRD performance (the capacity retention rate at 10C is 13.5%) compared with the master alloy and composite electrodes^{47,48}. Figure 3c compares the HRD performance of HSAs/NPNi composite and reported experimental data of AB₅-type HSAs from other advanced treatment methods, hot alkaline etching at 100 °C (KOH), electroless plating with Ni coating, and their combination for MmX_{4.3}(Al_{0.3}Mn_{0.4})_{0.5} (X = Co, Mo, Mn, Al, Cu)¹⁴, carbon nanotube (CNT) doping for MmNi_{3.6}Co_{0.7}Al_{0.3}Mn_{0.4}²⁷, fluoridation treatment, fluoridation and the following treatment with KBH₄ for MmNi_{3.8}Co_{0.75}Mn_{0.4}Al_{0.2}¹⁵, combination of fluoridation treatment and electroless plating with Ni-P coating for LaNi₄Al²⁵ etc. It can be seen that the HSAs/NPNi composite shows similar HRD performance as CNT-doped HSAs and notable superiority than other surface modification methods. Moreover, the incorporation of NPNi has better enhancement effect on the HRD properties of HSAs than CNT doping, especially when discharge current densities are larger than 1500 mA g⁻¹ as shown in Fig. 3d, which plots the ratios of their HRD property after treatment to that of untreated HSAs. On one hand, this is owing to the excellent contact between NPNi and HSAs in our composite, which is beneficial for decreases of the internal resistance and polarization. On the other hand, the NPNi provides numerous active sites for the adsorption of OH⁻ and also accelerates transfer rates of the electron and ion due to its unique three-dimensional bicontinuous structure, both of which are beneficial for the enhanced electrochemical reaction kinetics.

Figure 4 further compares the discharge capacity curves of master alloy electrode and HSAs/NPNi hybrid electrode at different discharge current densities of 1C, 5C, 8C and 10C. It is evident that the discharge capacities of the both electrodes decrease with increasing discharge rate. Although the composite electrode has lower discharge capacity than that of the master alloy electrode at 1C, it is quite the opposite at larger discharge rates (5C, 8C and 10C), which indicates the enhanced HRD properties of the composite electrode. Moreover, the discharge potential plateau of the composite electrode is higher than that of the master alloy electrode at each discharge rate, which demonstrates higher surface activity and smaller polarization of the former⁴⁹.

To explore the nature which underpins the superior HRD performance of the HSAs/NPNi hybrid electrode compared with bare HSAs electrode, we measured their linear polarization curves, electrochemical impedance spectra (EIS), anodic polarization curves and potential steps. Figure 5a presents linear polarization curves of the both electrodes. When the overpotential η changes within a small range (<10 mV), i.e. at a low overpotential, I_0 is given by:

$$I_0 = RTI_d/(F\eta) \quad (1)$$

where R , T , I_d and F denote the gas constant, the absolute temperature, the applied current density and the Faraday constant, respectively^{50–52}. From Table 1, the HSAs/NPNi hybrid electrode has a larger I_0 value (166.88 mA g⁻¹)

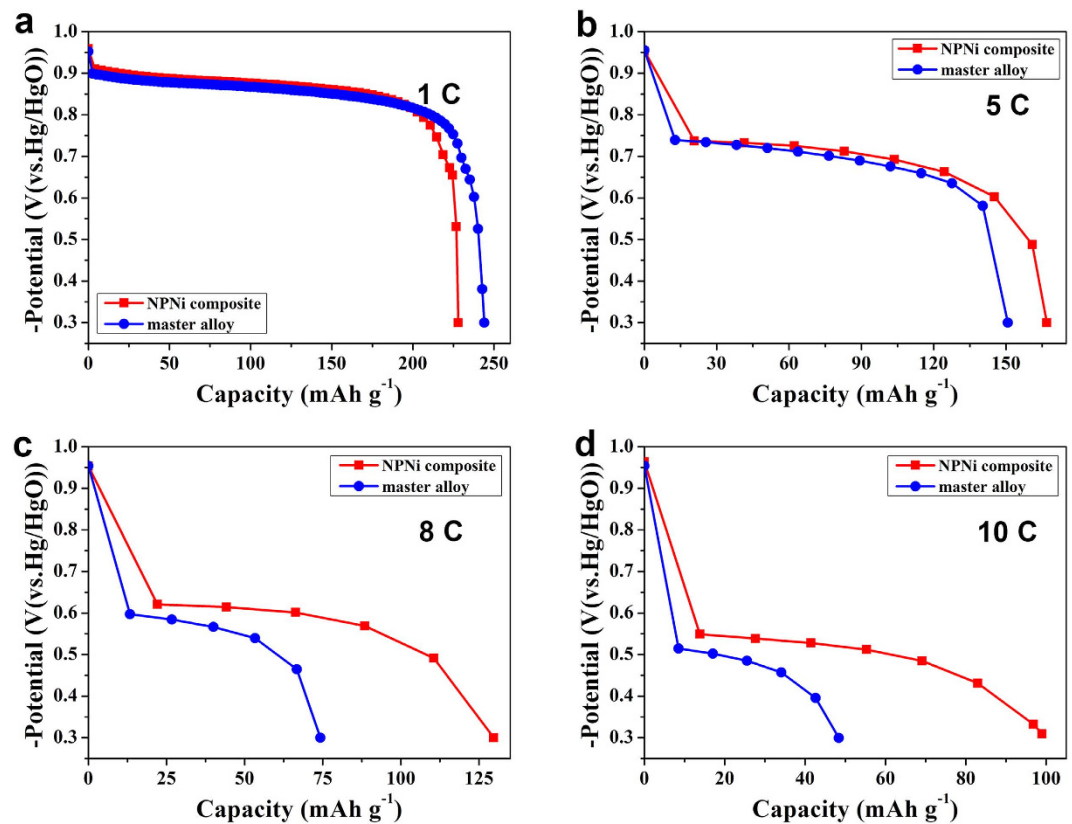


Figure 4. Discharge capacities of the HSAs/NPNi hybrid electrode and master alloy electrode at different discharge current densities. (a) 300 mA g^{-1} (1C), (b) 1500 mA g^{-1} (5C), (c) 2400 mA g^{-1} (8C) and (d) 3000 mA g^{-1} (10C).

than that of the master alloy electrode (104.22 mA g^{-1}), implying better hydrogen absorption and desorption kinetics of the former. The large surface/volume ratio and the unique three-dimensional bicontinuous structure of the NPNi enlarge the contact area between active materials and the electrolyte, accelerating the mass transportation rates of OH^- and H_{ads} ⁵³. The NPNi in the composites is not only a current collector, but also a bridge, which connects adjacent alloy particles to reduce the contact resistance. This can be characterized by the EIS results measured at a near-equilibrium state without damage to the samples as shown in Fig. 5b. It can be seen that each spectrum consists of two semicircles in the high-frequency region and a straight line in the low-frequency region. The small and large semicircles represent R_C and R_{CT} , respectively, while the straight line denotes the Warburg impedance relating to the diffusion^{34,55}. Note that the smaller the semicircle, the smaller the impedance. The R_C and R_{CT} values of the both electrodes can be obtained according to the equivalent circuit diagram in the figure⁵⁶, which are listed in Table 1. It is clear that the NPNi decreases R_C and R_{CT} , depressing the polarization (including resistance polarization and electrochemical polarization) of the hybrid electrode. This is caused by the unique three-dimensional bicontinuous nanostructure of the NPNi and the integration of NPNi and HSAs in the composite, which enable fast diffusion of reactants and products and also fast transfer of proton and electron. The above R_{CT} could also be used to calculate the I_0 value under a small-signal alternating current^{22,57}. The corresponding I_0 function is given by:

$$I_0 = RT/(FR_{CT}). \quad (2)$$

Based on Eq. (2), the calculated I_0 value of the composite electrode is 387.54 mA g^{-1} , which is larger than that of the master alloy electrode ($I_0 = 305.65 \text{ mA g}^{-1}$). It should be noted that the calculated I_0 values are much larger than those measured by the linear polarization curves. This is because the polarization resistance (η/I_d) determined by linear polarization curves is the sum of R_{CT} , ohmic resistance and diffusion resistance while the latter two terms cannot be neglected (they should be comparable with R_{CT} in this case)^{58,59}. Nonetheless, the data obtained from the both methods indicate that the composite electrode shows larger I_0 value than that of the master alloy electrode, validating the accuracy of our experimental results.

In addition to faster electrochemical kinetics, the hybrid electrode also exhibits faster hydrogen diffusion rate than that of the master alloy electrode. Figure 5c plots anodic polarization curves of the both electrodes. During the process of anodic polarization, the current density first increases with increasing overpotential and reaches a maximum value, which is defined as the limiting current density I_L . The I_L value is directly proportional to the hydrogen diffusion rate in the alloy bulk, i.e., the larger the I_L value, the faster the rate of hydrogen diffusion^{31,39}. The HSAs/NPNi hybrid electrode shows a larger I_L value ($3700.98 \text{ mA g}^{-1}$) than that of the master alloy electrode

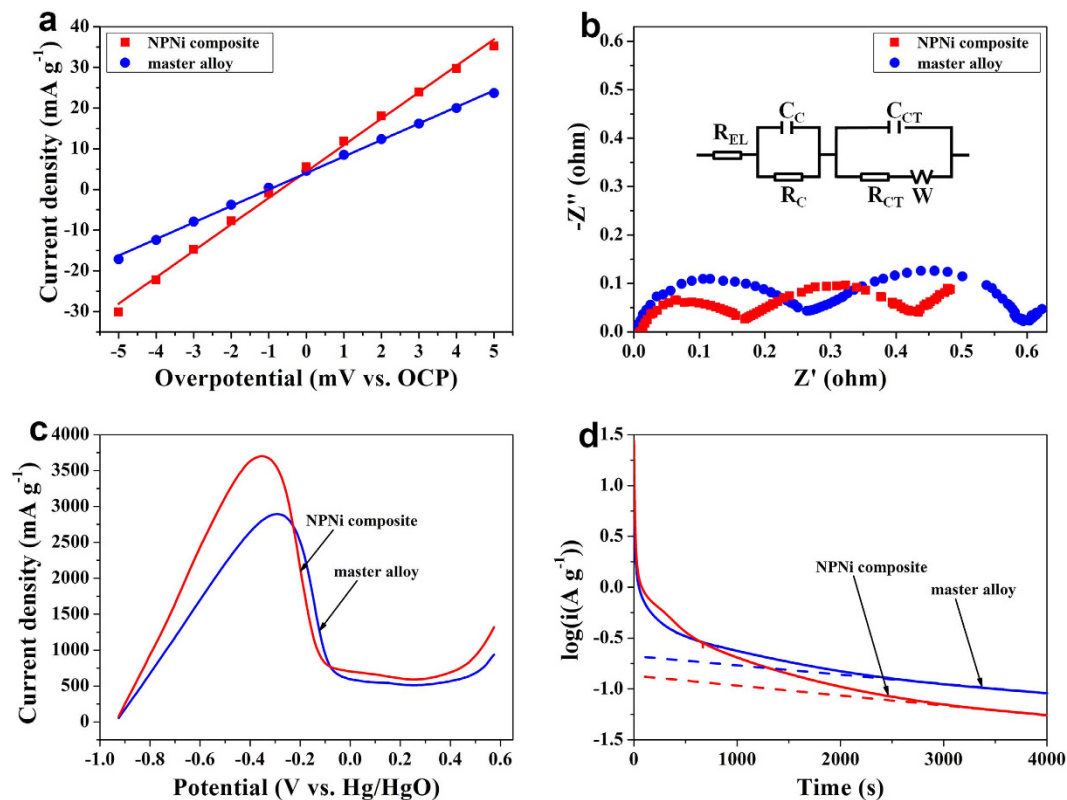


Figure 5. Electrochemical measurements results of the HSAs/NPNi hybrid electrode and master alloy electrode at room temperature. (a) Electrochemical impedance spectra at 50% DOD. (b) Linear polarization curves at 50% DOD. (c) Anodic polarization curves at 50% DOD. (d) Semilogarithmic curves of anodic current density versus discharge time at 100% state of charge.

(2894.90 mA g⁻¹) as listed in Table 1. Moreover, the diffusion rate of hydrogen can also be calculated by a potentiostatic method³¹ as illustrated in Fig. 5d. From the curves of discharge current density vs. discharge time, the current densities of the both electrodes decrease dramatically at first owing to the polarization (the concentration of hydrogen atoms on the alloy surface decreases obviously). Then, with increasing discharge time, the diffusion of hydrogen atoms in the alloy bulk becomes a rate-determination step and a linear relation exists between the semilogarithmic discharge current density and discharge time. In this case, the hydrogen diffusion coefficient D_H in the alloy bulk can be expressed by:

$$\log i = \log \left[\frac{6FD_H}{da^2} (C_0 - C_s) \right] - \frac{\pi^2 D_H}{2.303a^2} t \quad (3)$$

where i , d , a , C_0 , C_s , t are the anodic current density, the alloy density, the radius of alloy particles (=25 μm here), the initial hydrogen concentration in the alloy, the surface hydrogen concentration of alloy, and the discharge time, respectively^{31,60}. The D_H values can be determined from the slopes of lines in the figure because of the linear relations between $\log i$ and t . From Table 1, D_H of HSAs/NPNi hybrid electrode is $1.35 \times 10^{-10} \text{cm}^2 \text{s}^{-1}$, which is larger than that of the master alloy electrode ($1.19 \times 10^{-10} \text{cm}^2 \text{s}^{-1}$). Thus, more H_{ads} are oxidized on the surface of the hybrid electrode, providing a larger concentration gradient to facilitate the hydrogen atoms diffusion inside the hydride⁴⁵. Summarizing the above findings, it is found that both the faster electrochemical reaction rate on the electrode surface and faster hydrogen diffusion rate in the alloy bulk contribute to better HRD performance of the HSAs/NPNi hybrid electrode than that of the master alloy electrode.

Conclusions

In summary, we have developed a facile and scalable strategy to prepare the HSAs/NPNi hybrid electrode, which shows superior HRD performance than that of the bare alloy electrode. The capacity retention rate of the former (44.6%) is 2.4 times that of the latter (18.8%) at a discharge current density of 3000 mA g⁻¹. The unique three-dimensional bicontinuous nanostructure of NPNi in the composite substantially increases the charge transfer rate on alloy surface (higher I_0 and smaller R_{CT}) and hydrogen diffusion rate in alloy bulk (larger I_L and larger D_H). Moreover, the integration of HSAs and NPNi leads to a smaller R_C , effectively depressing the electrochemical polarization. The extraordinary performance of the hybrid electrode makes it a promising candidate for applications in high-power Ni-MH batteries. The top-down method in this work also provides a new strategy to enhance the HRD performance of other energy storage devices.

Methods

Figure 1 shows a schematic diagram of the procedure to prepare the HSAs/NPNi hybrid electrode pellet. The fabricating of the composite is carried out by using a top-down method, which involves hydrothermal synthesis of Ni(OH)₂⁶¹, integration of Ni(OH)₂ with the master alloy (LaCe)_{0.9}Y_{0.1}Ni_{3.7}Co_{0.75}(MnAl)_{0.65}, and the following annealing treatment, as illustrated in Fig. 1a. During the annealing process under an Ar/H₂ atmosphere, Ni(OH)₂ is reduced to nanoporous Ni since Ni(OH)₂ + H₂ → Ni + H₂O. Moreover, the annealing treatment also strengthens the interaction between the master alloy and NPNi⁶². Such a protocol can also be generalized towards the design and production of other HSAs/nanoporous metal composites. The electrode pellet with a diameter of 15 mm (Fig. 1b) is fabricated by cold pressing the mixture of as-prepared composite and carbonyl nickel powders. Typically, the electrode pellet is tied to a Ni-coated steel strip for electrochemical measurements³⁹. The experimental details are introduced below.

The master alloy (LaCe)_{0.9}Y_{0.1}Ni_{3.7}Co_{0.75}(MnAl)_{0.65} was prepared by inductive melting rare earth elements La, Ce, Y (99.5%) and other metallic elements Ni, Co, Mn, Al (99.9%) at an atmosphere of high-purity argon followed by annealing at 1000 °C for 5 h. As-annealed ingot was mechanically ground to powders. The average particle diameter of the powders is 50 ± 10 μm, which was measured by Malvern particle analyzer Mastersizer 2000. Ni(OH)₂, the precursor of NPNi, was fabricated by a simple hydrothermal method by adding the mixture of 1.45 g Ni(NO₃)₂, 1.4 g hexamethylenetetramine (HMT) and 35 ml ultrapure water into a Teflon-lined stainless autoclave⁶¹. After that, the sealed autoclave was heated in an electric oven at 100 °C for 10 h. After the autoclave was cooled to room temperature (25 °C), green products Ni(OH)₂ were collected by centrifugation. As-prepared HSAs powders and Ni(OH)₂ were then mixed and ground in an agate mortar. Subsequently, the mixture was dried in an electric oven and thermally reduced in a tube furnace at a temperature of 400 °C for 5 h under an Ar/H₂ atmosphere. Finally, we got black composite of HSAs and NPNi, where the mass fraction of NPNi was determined by ICP measurements. For a comparison study, the master alloy was also annealed under the same condition (at 400 °C for 5 h under an atmosphere of Ar/H₂) as the composite prior to compacting with carbonyl nickel powders.

The morphology and microstructure of specimens were investigated by an FESEM (JSM-6700F, JEOL, 15 keV) and a TEM (Tecnai, F20, FEI, 200 keV). Composition analysis was performed using an ICP analyzer. XRD measurements were tested using a D/max2500pc diffractometer with Cu K_α radiation.

The electrode pellets with a diameter of 15 mm were prepared by cold pressing the mixture of fabricated composite (or master alloy) and carbonyl nickel powder in a weight ratio of 1:4 under a pressure of 8 MPa. The electrochemical measurements were performed by using an Arbin BT-2000 battery test system at room temperature in a standard tri-electrode system, which was composed of a metal hydride electrode as working electrode, a sintered Ni(OH)₂/NiOOH electrode as counter electrode, and a Hg/HgO electrode as reference electrode, the electrolyte is 30% KOH solution. The electrodes were charged for 7.5 h at 60 mA g⁻¹ (the selected over-charging ratio of 50% is to ensure full charging of the MH electrode^{63–65}), and then discharged at 60 mA g⁻¹ to a cut-off potential of -0.3 V (vs. Hg/HgO). The maximum discharge capacity C_{max} was obtained after 4-cycle activation. After that, the electrodes were charged at 300 mA g⁻¹ for 1.5 h (the over-charging ratio is 50%) and then discharged at 300, 600, 900, 1200, 1500, 2400, 3000 mA g⁻¹ to a cut-off potential of -0.3 V (vs. Hg/HgO), respectively, to measure the discharge capacities (C_d) of electrodes at different discharge densities. The HRD performance is evaluated by:

$$HRD = C_d / C_{max} \times 100\%. \quad (4)$$

The electrochemical curves measurements were performed by using an IVIUM electrochemical analyzer at room temperature. EIS measurements were carried out in the frequency range from 100 kHz to 5 mHz with an amplitude of 5 mV vs. the open circuit potential (OCP) at 50% depth of discharge (DOD). The linear polarization curves measurements were conducted over the potential range from -5 to 5 mV (vs. OCP) at a scan rate of 0.05 mV s⁻¹. The anodic polarization curves were measured by sweeping the potential from 0 to 1.5 V (vs. OCP) at a scan rate of 5 mV s⁻¹ at 50% DOD. The potentiostatic experiments were performed at a potential step of +500 mV (vs. Hg/HgO) for 4000 s at 100% state of charge^{13,64}. Note that a higher potential of +500 mV was chosen to shorten the discharging time for obtaining a linear relationship between log*i* and *t*.

References

- Ovshinsky, S. R., Fetcenko, M. A. & Ross, J. A nickel metal hydride battery for electric vehicles. *Science* **260**, 176–181 (1993).
- Akimoto, H. Global air quality and pollution. *Science* **302**, 1716–1719 (2003).
- Davis, S. J., Caldeira, K. & Matthews, H. D. Future CO₂ emissions and climate change from existing energy infrastructure. *Science* **329**, 1330–1333 (2010).
- Schlapbach, L. & Züttel, A. Hydrogen-storage materials for mobile applications. *Nature* **414**, 353–358 (2001).
- Tarascon, J. M. & Armand, M. Issues and challenges facing rechargeable lithium batteries. *Nature* **414**, 359–367 (2001).
- Debe, M. K. Electrocatalyst approaches and challenges for automotive fuel cells. *Nature* **486**, 43–51 (2012).
- Taniguchi, A., Fujioka, N., Ikoma, M. & Ohta, A. Development of nickel/metal-hydride batteries for EVs and HEVs. *J. Power Sources* **100**, 117–124 (2001).
- Ye, H., Huang, Y., Chen, J. & Zhang, H. MmNi_{3.55}Co_{0.75}Mn_{0.4}Al_{0.3}B_{0.3} hydrogen storage alloys for high-power nickel/metal hydride batteries. *J. Power Sources* **103**, 293–299 (2002).
- Köhler, U., Kümpers, J. & Ullrich, M. High performance nickel-metal hydride and lithium-ion batteries. *J. Power Sources* **105**, 139–144 (2002).
- Dhar, S. K. *et al.* Nickel/metal hydride technology for consumer and electric vehicle batteries—a review and up-date. *J. Power Sources* **65**, 1–7 (1997).
- Fetcenko, M. A. *et al.* Recent advances in NiMH battery technology. *J. Power Sources* **165**, 544–551 (2007).
- Wang, G., Huang, J., Chen, S., Gao, Y. & Cao, D. Preparation and supercapacitance of CuO nanosheet arrays grown on nickel foam. *J. Power Sources* **196**, 5756–5760 (2011).
- Zhang, X., Sun, D., Yin, W., Chai, Y. & Zhao, M. Crystallographic and electrochemical characteristics of La_{0.7}Mg_{0.3}Ni_{3.5-x}(Al_{0.5}Mo_{0.5})_x (x = 0–0.8) hydrogen storage alloys. *J. Power Sources* **154**, 290–297 (2006).

14. Wu, M. S., Wu, H. R., Wang, Y. Y. & Wan, C. C. Surface treatment for hydrogen storage alloy of nickel/metal hydride battery. *J. Alloys Compd.* **302**, 248–257 (2000).
15. Zhao, X., Ma, L., Ding, Y., Yang, M. & Shen, X. Novel surface treatment for hydrogen storage alloy in Ni/MH battery. *Int. J. Hydrogen Energy* **34**, 3506–3510 (2009).
16. Liu, J. *et al.* Phase structure and electrochemical characteristics of high-pressure sintered La-Mg-Ni-based hydrogen storage alloys. *Electrochim. Acta* **111**, 18–24 (2013).
17. Zhang, L. *et al.* Phase transformation and cycling characteristics of a Ce₂Ni₇-type single-phase La_{0.78}Mg_{0.22}Ni_{3.45} metal hydride alloy. *J. Mater. Chem. A* **3**, 13679–13690 (2015).
18. Sakai, T., Ishikawa, H., Oguro, K., Iwakura, C. & Yoneyama, H. Effects of microencapsulation of hydrogen storage alloy on the performances of sealed nickel/metal hydride batteries. *J. Electrochem. Soc.* **134**, 558–562 (1987).
19. Sakai, T., Yuasa, A., Ishikawa, H., Miyamura, H. & Kuriyama, N. Nickel-metal hydride battery using microencapsulated alloys. *J. Less Common Met.* **172–174**, 1194–1204 (1991).
20. Iwakura, C., Matsuoka, M., Asai, K. & Kohno, T. Surface modification of metal hydride negative electrodes and their charge/discharge performance. *J. Power Sources* **38**, 335–343 (1992).
21. Zheng, G., Popov, B. N. & White, R. E. Determination of transport and electrochemical kinetic parameters of bare and copper-coated LaNi_{4.7}Sn_{0.24} electrodes in alkaline solution. *J. Electrochem. Soc.* **143**, 834–839 (1996).
22. Haran, B. S., Popov, B. N. & White, R. E. Studies on electroless cobalt coatings for microencapsulation of hydrogen storage alloys. *J. Electrochem. Soc.* **145**, 3000–3007 (1998).
23. Bai, A. & Hu, C. Effects of electroplating variables on the composition and morphology of nickel-cobalt deposits plated through means of cyclic voltammetry. *Electrochim. Acta* **47**, 3447–3456 (2002).
24. Raju, M., Ananth, M. V. & Vijayaraghavan, L. Influence of electroless coatings of Cu, Ni-P and Co-P on MmNi_{3.25}Al_{0.35}Mn_{0.25}Co_{0.66} alloy used as anodes in Ni-MH batteries. *J. Alloys Compd.* **475**, 664–671 (2009).
25. Zhao, X., Ma, L., Gao, Y., Ding, Y. & Shen, X. Effect of surface treatments on microstructure and electrochemical properties of La-Ni-Al hydrogen storage alloy. *Int. J. Hydrogen Energy* **34**, 1904–1909 (2009).
26. Ares, J. R., Cuevas, F. & Percheron-Guégan, A. Mechanical milling and subsequent annealing effects on the microstructural and hydrogenation properties of multisubstituted LaNi₅ alloy. *Acta Mater.* **53**, 2157–2167 (2005).
27. Li, S. *et al.* Electrochemical properties of MmNi_{3.6}Co_{0.7}Al_{0.3}Mn_{0.4} alloy containing carbon nanotubes. *J. Alloys Compd.* **353**, 295–300 (2003).
28. Huang, Z. G., Guo, Z. P., Calka, A., Wexler, D. & Liu, H. K. Effects of carbon black, graphite and carbon nanotube additives on hydrogen storage properties of magnesium. *J. Alloys Compd.* **427**, 94–100 (2007).
29. Chen, W. *et al.* Significantly improved electrochemical hydrogen storage properties of magnesium nickel hydride modified with nano-nickel. *J. Power Sources* **280**, 132–140 (2015).
30. Rao, Z. & Wang, S. A review of power battery thermal energy management. *Renew. Sustain. Energy Rev.* **15**, 4554–4571 (2011).
31. Liu, Y., Pan, H., Gao, M. & Wang, Q. Advanced hydrogen storage alloys for Ni/MH rechargeable batteries. *J. Mater. Chem.* **21**, 4743–4755 (2011).
32. Hou, C. *et al.* Integrated solid/nanoporous copper/oxide hybrid bulk electrodes for high-performance lithium-ion batteries. *Sci. Rep.* **3**, 2878 (2013).
33. Snyder, J., Asanithi, P., Dalton, A. B. & Erlebacher, J. Stabilized nanoporous metals by dealloying ternary alloy precursors. *Adv. Mater.* **20**, 4883–4886 (2008).
34. Zhang, J. & Li, C. M. Nanoporous metals: fabrication strategies and advanced electrochemical applications in catalysis, sensing and energy systems. *Chem. Soc. Rev.* **41**, 7016–7031 (2012).
35. Wittstock, a, Zielasek, V., Biener, J., Friend, C. M. & Baumer, M. Nanoporous gold catalysts for selective gas-phase oxidative coupling of methanol at low temperature. *Science* **327**, 319–322 (2010).
36. Zhu, C., Du, D., Eychmüller, A. & Lin, Y. Engineering ordered and nonordered porous noble metal nanostructures: synthesis, assembly, and their applications in electrochemistry. *Chem. Rev.* **115**, 8896–8943 (2015).
37. Zhu, G.-N. *et al.* Carbon-coated nano-sized Li₄Ti₅O₁₂ nanoporous micro-sphere as anode material for high-rate lithium-ion batteries. *Energy Environ. Sci.* **4**, 4016–4022 (2011).
38. Qiu, H.-J. *et al.* Fabrication of large-scale nanoporous nickel with a tunable pore size for energy storage. *J. Power Sources* **247**, 896–905 (2014).
39. Kleperis, J. *et al.* Electrochemical behavior of metal hydrides. *J. Solid State Electrochem.* **5**, 229–249 (2001).
40. Iwakura, C., Matsuoka, M., Asai, K. & Kohno, T. Surface modification of metal hydride negative electrodes and their charge/discharge performance. *J. Power Sources* **38**, 335–343 (1992).
41. Hu, W.-K. *et al.* Annealing effect on phase composition and electrochemical properties of the Co-free La₂MgNi₉ anode for Ni-metal hydride batteries. *Electrochim. Acta* **96**, 27–33 (2013).
42. Chen, C. *et al.* B₂O₃-based composite to rival polycrystalline cubic boron nitride. *Adv. Mater.* **19**, 4288–4291 (2007).
43. Liu, P., Ge, X., Wang, R., Ma, H. & Ding, Y. Facile fabrication of ultrathin Pt overlayers onto nanoporous metal membranes via repeated Cu UPD and *in situ* redox replacement reaction. *Langmuir* **25**, 561–567 (2009).
44. Fujita, T. *et al.* Atomic origins of the high catalytic activity of nanoporous gold. *Nat. Mater.* **11**, 775–780 (2012).
45. Iwakura, C., Matsuoka, M. & Kohno, T. Mixing effect of metal oxides on negative electrode reactions in the nickel-hydride battery. *J. Electrochem. Soc.* **141**, 2306–2309 (1994).
46. Metikoš-Huković, M., Grubač, Z., Radić, N. & Tonejc, A. Sputter deposited nanocrystalline Ni and Ni-W films as catalysts for hydrogen evolution. *J. Mol. Catal. A Chem.* **249**, 172–180 (2006).
47. Schober, T. On the activation of FeTi for hydrogen storage. *J. Less Common Met.* **89**, 63–70 (1983).
48. Buschow, K. H. J. “Hydrogen absorption in intermetallic compounds” In *Handbook on the physics and chemistry of rare earths* Vol. 6 (eds. Gschneidner, K. A. *et al.*) Ch. 47, 1–28 (Elsevier, 1984).
49. Ouyang, L. Z. *et al.* Enhanced high-rate discharge properties of La_{11.3}Mg_{6.0}Sm_{7.4}Ni_{61.0}Co_{7.2}Al_{7.1} with added graphene synthesized by plasma milling. *Int. J. Hydrogen Energy* **39**, 12765–12772 (2014).
50. Yayama, H., Hirakawa, K. & Tomokiyo, A. Equilibrium potential and exchange current density of metal hydride electrode. *Jpn. J. Appl. Phys.* **25**, 739–742 (1986).
51. Notten, P. H. L. & Hokkelling, P. Double-phase hydride forming compounds: a new class of highly electrocatalytic materials. *J. Electrochem. Soc.* **138**, 1877–1885 (1991).
52. Senoh, H., Morimoto, K., Inoue, H., Iwakura, C. & Notten, P. H. L. Relationship between equilibrium hydrogen pressure and exchange current for the hydrogen electrode reaction at MmNi_{3.9-x}Mn_{0.4}Al_xCo_{0.7} alloy electrodes. *J. Electrochem. Soc.* **147**, 2451–2455 (2000).
53. Bell, A. T. The impact of nanoscience on heterogeneous catalysis. *Science* **299**, 1688–1691 (2003).
54. Lundqvist, A. & Lindbergh, G. Kinetic study of a porous metal hydride electrode. *Electrochim. Acta* **44**, 2523–2542 (1999).
55. Valøen, L. O., Lasa, A., Jensen, J. O. & Tunold, R. The electrochemical impedance of metal hydride electrodes. *Electrochim. Acta* **47**, 2871–2884 (2002).
56. Iwakura, C., Oura, T., Inoue, H., Matsuoka, M. & Yamamoto, Y. Effect of alloy composition on hydrogen diffusion in the AB₅-type hydrogen storage alloys. *J. Electroanal. Chem.* **398**, 37–41 (1995).
57. Wang, C. Kinetic behavior of metal hydride electrode by means of AC impedance. *J. Electrochem. Soc.* **145**, 1801–1812 (1998).

58. Wang, C., Soriaga, M. P. & Srinivasan, S. Determination of reaction resistances for metal-hydride electrodes during anodic polarization. *J. Power Sources* **85**, 212–223 (2000).
59. Yuan, A. & Xu, N. A study on the effect of nickel, cobalt or graphite addition on the electrochemical properties of an AB₅ hydrogen storage alloy and the mechanism of the effects. *J. Alloys Compd.* **322**, 269–275 (2001).
60. Zheng, G., Popov, B. N. & White, R. E. Electrochemical determination of the diffusion coefficient of hydrogen through an LaNi_{4.25}Al_{0.75} electrode in alkaline aqueous solution. *J. Electrochem. Soc.* **142**, 2695–2698 (1995).
61. Lu, Z., Chang, Z., Zhu, W. & Sun, X. Beta-phased Ni(OH)₂ nanowall film with reversible capacitance higher than theoretical faradic capacitance. *Chem. Commun.* **47**, 9651–9653 (2011).
62. Cai, A., Zhang, H., Hua, H. & Zhang, Z. Direct formation of self-assembled nanoporous aluminium oxide on SiO₂ and Si substrates. *Nanotechnology* **13**, 627–630 (2002).
63. Zhang, Y. *et al.* Microstructure and electrochemical characteristics of Mm(Ni,Co,Mn,Al)₅B_x ($x = 0-0.4$) hydrogen storage alloys prepared by cast and rapid quenching. *Electrochim. Acta* **49**, 1161–1168 (2004).
64. Zhang, W. *et al.* Study on kinetics and electrochemical properties of low-Co AB₅-type alloys for high-power Ni/MH battery. *Electrochim. Acta* **54**, 1383–1387 (2009).
65. Shen, W., Han, S., Li, Y., Song, J. & Tong, Q. Study on surface modification of AB₅-type alloy electrode with polyaniline by electroless deposition. *Electrochim. Acta* **56**, 959–963 (2010).

Acknowledgements

We wish to thank ChangBai Mountain Scholars Program, Natural Science Foundation of Jilin Province (No. 20160101315JC) and Jilin University Basic Research Grants Program for financially supporting this project.

Author Contributions

M.M.L., C.C.Y. and Q.J. conceived and designed the experiments. M.M.L., C.C.Y. and C.C.W. carried out the fabrication of materials and performed electrochemical measurements. Z.W. and Y.F.Z. contributed to the microstructural characterizations. M.Z., J.C.L., W.T.Z. and J.S.L. provided helps in the experiments. M.M.L., C.C.Y. and Q.J. wrote the paper, and all authors discussed the results and commented on the manuscript.

Additional Information

Competing financial interests: The authors declare no competing financial interests.

How to cite this article: Li, M. M. *et al.* Design of Hydrogen Storage Alloys/Nanoporous Metals Hybrid Electrodes for Nickel-Metal Hydride Batteries. *Sci. Rep.* **6**, 27601; doi: 10.1038/srep27601 (2016).



This work is licensed under a Creative Commons Attribution 4.0 International License. The images or other third party material in this article are included in the article's Creative Commons license, unless indicated otherwise in the credit line; if the material is not included under the Creative Commons license, users will need to obtain permission from the license holder to reproduce the material. To view a copy of this license, visit <http://creativecommons.org/licenses/by/4.0/>